A Fisheye Camera System for Polarisation Detection on UAVs

Wolfgang Stürzl[1,2] and Nicole Carey[2]

[1] Institute of Robotics and Mechatronics, German Aerospace Center (DLR)
[2] Center of Excellence Cognitive Interaction Technology
and Department of Neurobiology, Bielefeld University, Germany
wolfgang.stuerzl@dlr.de, nicole.carey@uni-bielefeld.de

Abstract. We present a light-weight polarisation sensor that consists of four synchronised cameras equipped with differently oriented polarisers and fisheye lenses allowing us to image the whole sky hemisphere. Due to its low weight and compact size it is well-suited as a biomimetic sensor on-board a UAV. We describe efficient methods for reconstruction of the full-sky polarisation pattern and estimation of sun position. In contrast to state-of-the art polarisation systems for UAVs that estimate sun azimuth only, our approach can determine sun elevation as well, even in the presence of clouds and for significant pitch and roll angles of the UAV. The calibration and registration of the four fisheye cameras is achieved by extending an existing omni-directional calibration toolbox to multi-camera calibration. We present examples of full-sky reconstruction of the polarisation pattern as well as an analysis of the error in the sun position estimate. In addition, we performed a preliminary test on-board a quadcopter.

1 Introduction

The polarisation pattern in the sky is caused by scattering of sunlight in the atmosphere of the earth. Since it is symmetrical with respect to the observer–sun axis it can be used as a compass cue and it has long been known that skylight polarisation is used by insects for navigation [1–3]. In this paper we present a compact sensor that is well-suited to enable polarisation-based navigation of small UAVs or mobile robots. Due to its large field of view it also allows detailed full-sky reconstruction of the polarisation pattern.

Previous implementations of detailed full-sky polarimetry, notably Gal et al. [4], North and Duggin [5], Voss and Liu [6], and Miyazaki et al [7] have been large and require rotation of the polariser, making them not suited to implementation on small autonomous vehicles, much less flying ones. Conversely, mobile platforms employing polarisation detection such as that described by Lambrinos et al [8], Pandian [9] and Chahl and Mizutani [10] tend to have narrower viewing fields, and are more interested in gross attitude estimation than reconstructing the finer structure of the polarisation properties of the sky hemisphere and landscape.

A. Fusiello et al. (Eds.): ECCV 2012 Ws/Demos, Part II, LNCS 7584, pp. 431–440, 2012.

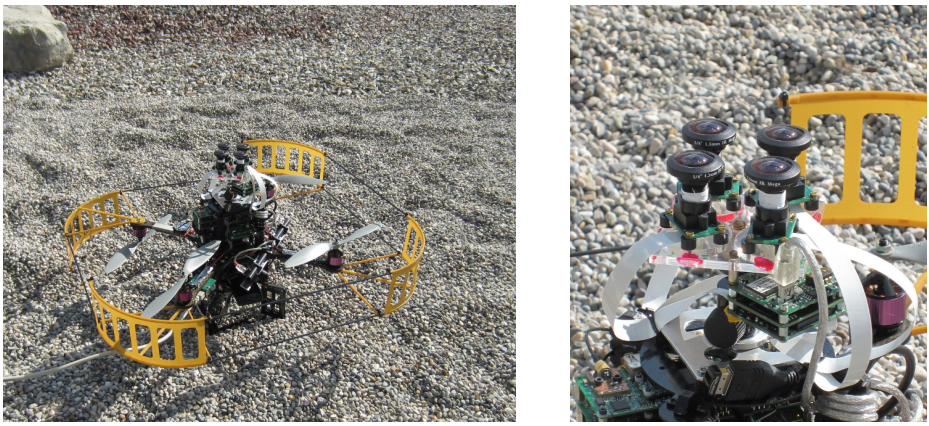

Fig. 1. The four-camera polarisation sensor mounted on a quadrotor (AscTec Pelican)

2 Polarisation Sensor and Calibration

Fig. 1 shows our wide-angle polarisation sensor consisting of four small camera units with fisheye lenses. Each is equipped with a differently oriented polariser placed between lens and CMOS sensor. Images are captured synchronously and transmitted serially via USB 2.0 by means of a multi-sensor board (VRmMFC, VRmagic).

2.1 Intensity and Polariser Orientation Calibration

If placed behind a linear polariser oriented at angle ϕ_k, the response of the camera sensor to partially linearly polarised light is given by [11]

$$I = f[Q_0(1 + \delta\cos(2\phi - 2\phi_k))] \ , \tag{1}$$

where Q_0 is the energy of the unpolarised light absorbed by a sensor pixel during camera exposure, δ its degree of polarisation and ϕ its polarisation angle. In the simplest case, the function $f[]$ consists of a linear gain followed by analog-to-digital conversion, which we disregard in the following,

$$I = g\,Q_0\,(1 + \delta\cos(2\phi - w\phi_k)) \ . \tag{2}$$

To estimate the polariser orientation, we used a known polarised light source – an LCD computer monitor set to display a simple white background – and using a relatively long exposure (to maximise the sensitivity to minor intensity changes) we rotated the camera system around its central axis in increments of one degree. We then calculated the mean intensity of a central group of pixels for each camera at each rotational position. The angle corresponding to the lowest mean intensity was assumed to be the long anti-preferred axis of the polariser.

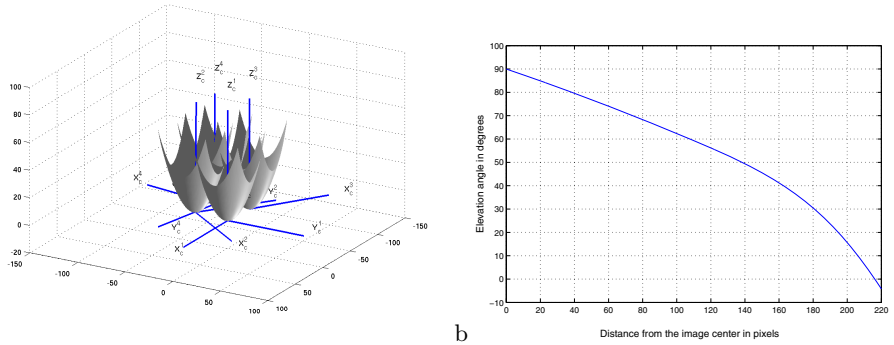

a b

Fig. 2. a) Illustration of the estimated poses of the four fisheye cameras. b) Radial mapping function of camera 1.

To calibrate the intensity gain function for the cameras, we used the same light source and conducted four independent calibrations with the screen aligned with the centre of the viewing angle of the camera being calibrated. We also ensured that each camera had the same polariser orientation relative to the screen, and increased the exposure time gradually. In this way, we could verify that the gain function of each camera was linear across the image, and adjust for any discrepancies in the slopes of the different cameras.

Remark: We did not compensate for "radial intensity fall-off" induced by the fisheye lenses, since we were mainly interested in polarisation angle and degree of polarisation and not intensity.[1] All four lenses were assumed to have very similar fall-off functions and for estimating polarisation, similar positions in the four cameras are used.

2.2 Geometrical Calibration: Intrinsic Camera Parameters and Registration of Reference Frames

In order to obtain a full calibration of the four fisheye cameras, i.e. estimation of four sets of intrinsic camera parameters and rigid-body transformations between the camera reference frames, we extended the "Omnidirectional Camera Calibration Toolbox (OCamCalib)" [12] to multi-camera calibration. In addition to providing transformation parameters, our approach improves the estimation of intrinsic camera parameters since the number of necessary pose estimations of the calibration board per camera is reduced.[2]

[1] Radial intensity fall-off can be modelled by a multiplicative function.

[2] If N_I is the number of images per camera used for calibration and N_{ip} the number of internal parameters per camera, then we have to estimate just $4 \times N_{\text{ip}} + (N_I + 3) \times 6$ parameters compared with $4 \times N_{\text{ip}} + N_I \times 4 \times 6$ parameters when using the single-camera calibration framework for each of the four cameras.

a 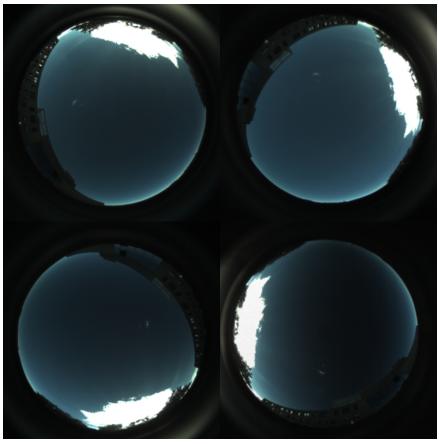 b 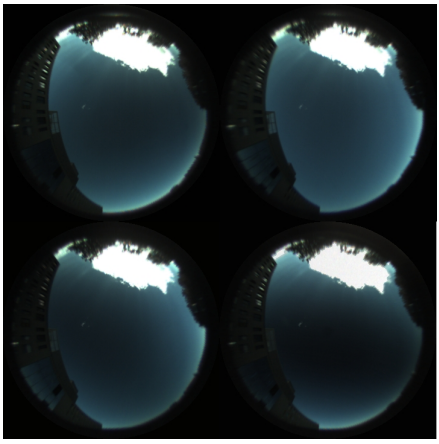

Fig. 3. Using the calibration results, the four cameras images shown in (a) are remapped to the same orientation and with corresponding pixels having identical viewing directions (b). An equidistant angular mapping is employed radially, i.e. the elevation angle depends linearly on the distance from the image center, el $= 90^\circ - k\sqrt{(u-u_c)^2+(v-v_c)^2}$.

The estimated relative poses of the four camera reference frames and a typical radial mapping function (elevation angle in dependence on the distance from the estimated image center in pixels) are shown in Fig. 2. For the calibration, we used 10 sets of four synchronously captured images and a 4th order polynomial for the radial projection function.

As shown in Fig. 3, after geometrical calibration, the four simultaneously captured camera images can be remapped in such a way that each viewing direction corresponds to the same pixel coordinates in each of the four remapped images.

3 Estimating Local Polarisation

After calibration of the four camera system, the polarisation angle ϕ and the degree of polarisation δ for each viewing direction can be estimated from the pixel values I_k of the $K = 4$ sensors by minimising the following error function, deduced from Eq. (2):

$$\begin{aligned} E(A,B,Q_0) &= \sum_{k=1}^{K} \left(Q_0(1+\delta\cos(2\phi-2\phi_k)) - g_k^{-1}I_k\right)^2 \\ &= \sum_{k} \left(Q_0 + Q_0\delta\left(\cos(2\phi)\cos(2\phi_k)+\sin(2\phi)\sin(2\phi_k)\right) - g_k^{-1}I_k\right)^2 \\ &= \sum_{k} \left(Q_0 + Ac_k + Bs_k - J_k\right)^2 \quad , \end{aligned} \tag{3}$$

where we have substituted $A = Q_0\delta\cos(2\phi)$, $B = Q_0\delta\sin(2\phi)$, $c_k = \cos(2\phi_k)$, $s_k = \sin(2\phi_k)$, and $J_k = g_k^{-1}I_k$.

$$0 = \frac{\partial}{\partial Q_0}E(\phi,\delta,Q_0) \quad \Longrightarrow \quad Q_0^* = \bar{J} - A\bar{c} - B\bar{s} \ , \tag{4}$$

where $\bar{c} = \frac{1}{K}\sum c_k$, $\bar{s} = \frac{1}{K}\sum s_k$ and $\bar{J} = \frac{1}{K}\sum J_k$. Substituting this into (3),

$$\tilde{E}(A,B) = E(A,B,Q_0^*) = \sum_k \Big(A\tilde{c}_k + B\tilde{s}_k - \tilde{J}_k\Big)^2 \ , \tag{5}$$

where $\tilde{c}_k = c_k - \bar{c}$, $\tilde{s}_k = s_k - \bar{s}$, $\tilde{J}_k = J_k - \bar{J}$.

The solution of $0 = \frac{\partial}{\partial A}\tilde{E}(A,B)$ and $0 = \frac{\partial}{\partial B}\tilde{E}(A,B)$ is

$$A = \frac{N_A}{D_{AB}} \ , \quad B = \frac{N_B}{D_{AB}} \ , \tag{6}$$

$$N_A = \overline{\tilde{s}^2}\,\overline{\tilde{c}\tilde{J}} - \overline{\tilde{c}\tilde{s}}\,\overline{\tilde{s}\tilde{J}} \ , \quad N_B = \overline{\tilde{c}^2}\,\overline{\tilde{s}\tilde{J}} - \overline{\tilde{c}\tilde{s}}\,\overline{\tilde{c}\tilde{J}} \ , \quad D_{AB} = \overline{\tilde{c}^2}\,\overline{\tilde{s}^2} - \overline{\tilde{c}\tilde{s}}^2 \ , \tag{7}$$

where $\overline{\tilde{s}^2} = \frac{1}{K}\sum(s_k - \bar{s})^2$, $\overline{\tilde{c}^2} = \frac{1}{K}\sum(c_k - \bar{c})^2$, $\overline{\tilde{c}\tilde{s}} = \frac{1}{K}\sum(c_k - \bar{c})(s_k - \bar{s})$, $\overline{\tilde{c}\tilde{J}} = \frac{1}{K}\sum(c_k - \bar{c})(J_k - \bar{J})$, $\overline{\tilde{s}\tilde{J}} = \frac{1}{K}\sum(s_k - \bar{c})(J_k - \bar{J})$.

From A and B we can estimate the polarisation angle,

$$\tan(2\phi) = \frac{B}{A} = \frac{N_B}{N_A} \quad \Longrightarrow \quad \phi = \tfrac{1}{2}\mathrm{atan2}(N_B, N_A) \tag{8}$$

and the degree of polarisation

$$\delta = \frac{\sqrt{A^2+B^2}}{Q_0} = \frac{\sqrt{A^2+B^2}}{\bar{J} - A\bar{c} - B\bar{s}} = \frac{\sqrt{N_A^2+N_B^2}}{D_{AB}\bar{J} - N_A\bar{c} - N_B\bar{s}} \ . \tag{9}$$

Note that if the angles of the K polarisers are equally distributed, i.e. $\phi_k = \frac{k-1}{K}180^\circ + \phi_1$, $k = 1, 2, \ldots, K$, then the equations above are simplified to be[3]

$$A = \frac{2}{K}\sum_k \cos(2\phi_k)J_k \ , \quad B = \frac{2}{K}\sum_k \sin(2\phi_k)J_k \ , \tag{10}$$

$$\phi = \tfrac{1}{2}\mathrm{atan2}\Big(\sum_k \sin(2\phi_k)J_k, \sum_k \cos(2\phi_k)J_k\Big) \ , \tag{11}$$

$$\delta = \frac{2\sqrt{(\sum_k \cos(2\phi_k)J_k)^2 + (\sum_k \sin(2\phi_k)J_k)^2}}{\sum_k J_k} \ . \tag{12}$$

Finally, the polarisation angle with respect to the local meridian in the camera centered reference frame is computed,

$$\alpha[u,v] = \phi[u,v] - \mathrm{az}[u,v] \ . \tag{13}$$

[3] ϕ_1 is the orientation angle of the polariser in the first camera with respect to the camera reference frame.

The polarisation vector in 3D for a viewing direction given by azimuth angle 'az' and elevation angle 'el' is then

$$\boldsymbol{p}[u,v] = \cos(\alpha[u,v])\boldsymbol{e}_{\mathrm{el}}[u,v] + \sin(\alpha[u,v])\boldsymbol{e}_{\mathrm{az}}[u,v] \ , \tag{14}$$

where $\boldsymbol{e}_{\mathrm{el}} = \frac{\partial \boldsymbol{e}}{\partial \mathrm{el}} = (-\sin(\mathrm{el})\cos(\mathrm{az}), -\sin(\mathrm{el})\sin(\mathrm{az}), \cos(\mathrm{el}))^\top$, $\boldsymbol{e}_{\mathrm{az}} = \frac{1}{\cos(\mathrm{el})}\frac{\partial \boldsymbol{e}}{\partial \mathrm{az}}$ $= (-\sin(\mathrm{az}), \cos(\mathrm{az}), 0)^\top$, and $\boldsymbol{e} = (\cos(\mathrm{el})\cos(\mathrm{az}), \cos(\mathrm{el})\sin(\mathrm{az}), \sin(\mathrm{el}))^\top$ is the unit vector pointing into the direction given by (az, el).

4 Estimation of Sun Position from Polarisation

According to the single-scattering Rayleigh model, all polarisation vectors are orthogonal to the sun direction vector $\boldsymbol{e}_S$, i.e. $\boldsymbol{p}[u,v]^\top \boldsymbol{e}_S = 0$ for all u, v. We thus estimate the sun direction by minimising the deviation from orthogonality, i.e.

$$E(\boldsymbol{e}_S, \lambda) = \sum_{uv} w[u,v](\boldsymbol{p}[u,v]^\top \boldsymbol{e}_S)^2 - \lambda(\|\boldsymbol{e}_S\|^2 - 1) \ . \tag{15}$$

$w[u,v]$ is an optional weighting factor that can be set, for instance, proportional to the degree of polarisation $\delta[u,v]$, and the term $-\lambda(\|\boldsymbol{e}_S\|^2 - 1)$ ensures that $\boldsymbol{e_s}$ is a unit vector. Minimising (15) leads to

$$\lambda \boldsymbol{e}_S = \sum_{uv} w[u,v]\boldsymbol{p}[u,v]\boldsymbol{p}[u,v]^\top \boldsymbol{e}_S \ . \tag{16}$$

Thus, $\boldsymbol{e}_S$ is eigenvector of matrix $P = \sum_{uv} w[u,v]\boldsymbol{p}[u,v]\boldsymbol{p}[u,v]^\top$ corresponding to the smallest eigenvalue $\lambda_{\min}$.

4.1 Direct Estimation of Sun Azimuth

In case only the azimuthal angle of the sun is of interest, we can simplify our approach by projection onto the x-y plane, i.e. $\boldsymbol{p}[u,v]) = (p_x[u,v]), p_y[u,v]))^\top$, $\boldsymbol{e}[u,v]) = (e_x[u,v]), e_y[u,v]))^\top = (\cos(\mathrm{el}[u,v])\cos(\mathrm{az}[u,v]), \cos(\mathrm{el}[u,v])\sin(\mathrm{az}[u,v]))^\top$, $\boldsymbol{e}_S = (e_{xS}, e_{yS})^\top$, and minimise

$$E(\boldsymbol{e}_S) = \sum_{uv} w[u,v]\Big(\boldsymbol{p}[u,v]^\top(\boldsymbol{e}[u,v] - \boldsymbol{e}_S)\Big)^2 \ . \tag{17}$$

Note that in the 3-dimensional case, (17) is equivalent to (15) since $\boldsymbol{p}[u,v]^\top \boldsymbol{e}[u,v] = 0$. The explicit solution of (17) is given by

$$\begin{aligned}
e_S &= D^{-1}(N_x, N_y)^\top \ , \qquad (18)\\
N_x &= (\sum w[u,v]p_y^2[u,v])P_x - (\sum w[u,v]p_x[u,v]p_y[u,v])P_y \ ,\\
N_y &= (\sum w[u,v]p_x^2[u,v])P_y - (\sum w[u,v]p_x[u,v]p_y[u,v])P_x \ ,\\
P_x &= \sum w[u,v](\boldsymbol{p}[u,v]^\top \boldsymbol{e}[u,v])p_x[u,v] \ , \ P_y = \sum w[u,v](\boldsymbol{p}[u,v]^\top \boldsymbol{e}[u,v])p_y[u,v] \ ,\\
D &= (\sum w[u,v]p_{xi}^2)(\sum w[u,v]p_{yi}^2) - (\sum w[u,v]p_{xi}p_{yi})^2 \ .
\end{aligned}$$

and thus $\mathrm{azi}_S = \mathrm{atan2}(N_y, N_x)$.

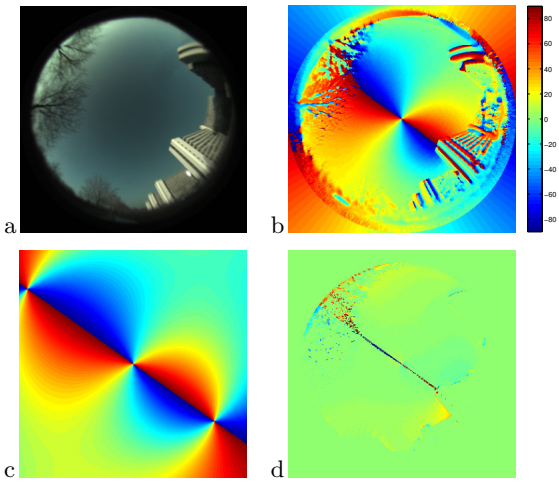

Fig. 4. Comparison of sky polarisation reconstructed using our four-lens system and the theoretical pattern predicted by the single-scatter model for the same sun placement. a) Remapped image of camera 1. b) Corresponding sky reconstruction with polarisation direction mapped to colour. c) Single-scatter polarisation model for the same sun position. d) Error between theoretical and estimated polarisation map.

4.2 Sky Reconstruction and Sun-Finding

Strictly speaking, the above method has two possible solutions under the single-scattering model: one at the sun position, and one diametrically opposite at the anti-solar position. However it is relatively trivial to distinguish between these possibilities; one may use the gravity vector to determine the most likely sun candidate, the chromatic gradient of the relative blue intensity of the sky [13], or even a simple intensity calculation.

In figure 4 we compare the sky pattern resolved by our sensor system with that predicted by the single scatter polarization model. The two are closely aligned (Fig. 4d) apart from some minor discrepancies. Using sky maps of this form, we tested our sun finding algorithm at various times of day. The results can be seen in figure 5. The azimuthal angle is resolved very precisely; the elevation estimation has a wider variance, possibly due to a higher sensitivity to atmospheric distortion [14].

Note that a more accurate sky model can be obtained via a double scattering formula [14], however our investigations showed the error between model and sky was not significantly reduced by incorporating these additional neutral points; moreover the inversion required to find the sun position becomes significantly more laborious.

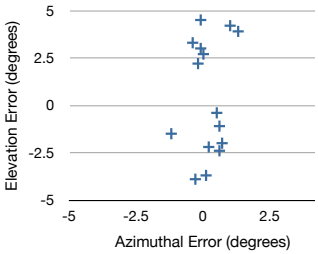

Fig. 5. Azimuth and elevational error in the sun-finding algorithm when tested on 15 images on a clear day. The sun was not visible due to horizon obstruction, but its position could be calculated based on the time, date, and lat./long. of the experimental location (Bielefeld, March 2012)

5 Discussion

The lightweight and speedy nature of this imaging system makes it well-suited to implementation on UAVs or small ground-based robots. Moreover, the wide-field visual sensors mean we can obtain a very accurate impression of the polarisation properties of natural scenes. This makes the system ideal for biomimetic investigations, such as tracing insect paths through canopied areas or cluttered environments, and reconstructing their visual input. Figure 6 demonstrates a sequence of images reconstructed from the system moving along a simulated 'bee-path' under a tree canopy. The sun is not visible and is difficult to pinpoint based on pure intensity information, however the sky pattern is clear even under hazy, nonoptimal conditions.

We also tested our polarisation sensor mounted on a quadcopter and compared the estimations from the sun finding algorithms described in section 4

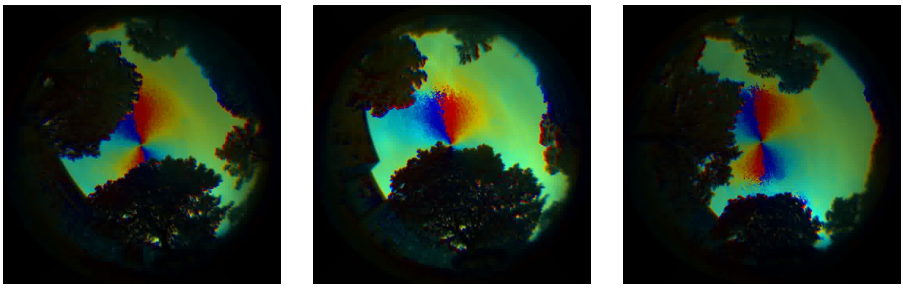

Fig. 6. Extracts from video footage taken on a hazy evening under heavy canopy. The poor atmospheric conditions attenuate the polarisation pattern around the horizon, however through gaps in the foliage around the zenith point, the solar meridian is clear and distinct.

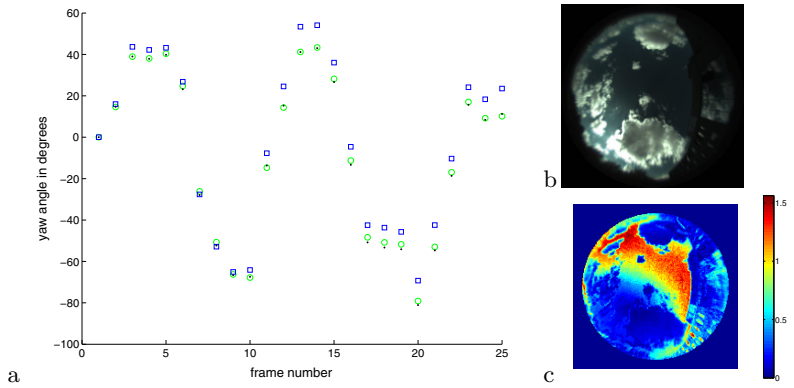

Fig. 7. a) Comparison of estimated yaw angles. Shown are values from the on-board IMU (squares), azimuth values of the sun vector calculated using either the eigenvector method described in section 4 (circles) or the direct approach, section 4.1 (dots). b) The first image of the sequence (remapped image of camera 1). c) The corresponding weight map $w[u, v]$. The weighting function was chosen to be $w[u, v] = B[u, v]/(R[u, v] + 1) \times \delta[u, v] \times \theta(\text{ele}[u, v] > 10^\circ)$, where $B[u, v]$ and $R[uv]$ are the blue and red pixel values at position $[u, v]$, $\delta[u, v]$ the degree of polarisation and $\theta(\text{ele}[u, v] > 10^\circ)$ is a step function that is $= 1$ for elevation angle larger than 10° and $= 0$ otherwise.

with yaw angle estimations of the on-board IMU. The results of 25 yaw-angle estimates during a 35 s segment of a flight with significant yaw-turns are shown in figure 7a. The flight was performed on a sunny day with clouds (see Fig. 7b). To reduce the effect of clouds, which can disrupt the polarisation pattern of the sky, we applied a weighting function that emphasises bluish parts with strong polarisation (Fig. 7c). The IMU data was obtained by interpolating the estimations from the quadcopter's autopilot that were recorded with 10 Hz. While the overall course matches, there a noticeable differences in the yaw value estimates between the IMU and the polarisation sensor. As the autopilot had no magnetic compass, slight drift in the yaw angle estimate might have occurred.

An integration of our polarisation system with other sensors on the quadcopter, in particular the IMU, is planned for future work.

Acknowledgements. We thank Michal Smíšek and Klaus Strobl for help with the extension of the calibration toolbox.

References

1. von Frisch, K.: The Dance Language and Orientation of Bees. Harvard University Press (1967)
2. Wehner, R.: Polarized-light navigation by insects. Scientific American 235, 106–115 (1976)

3. Srinivasan, M.V.: Honeybees as a model for the study of visually guided flight, navigation, and biologically inspired robotics. Physiological Reviews 91, 413–460 (2011)
4. Gal, J., Horvath, G., Meyer-Rochow, V.B., Wehner, R.: Polarization patterns of the summer sky and its neutral points measured by full-sky imaging polarimetry in finnish lapland north of the arctic circle. Proceedings of the Royal Society of London A 457, 1385–1399 (2001)
5. North, J.A., Duggin, M.J.: Stokes vector imaging of the polarized sky-dome. Applied Optics 36, 723–730 (1997)
6. Voss, K.J., Liu, Y.: Polarized radiance distribution measurements of skylight i. System description and characterisation. Applied Optics 36, 6083–6094 (1997)
7. Miyazaki, D., Ammar, M., Kawakami, R., Ikeuchi, K.: Estimating sunlight polarization using a fish-eye lens. IPSJ Transactions on Computer Vision and Applications 1, 288–300 (2009)
8. Lambrinos, D., Kobayash, H., Pfeifer, R., Maris, M., Labhart, T., Wehner, R.: An autonomous agent navigating with a polarized light compass. Adaptive Behavior 6, 131–161 (1997)
9. Pandian, A.: Robot navigation using stereo vision and polarization imaging, Masters Thesis, Institut Universitaire de Technologie IUT Le Creusot, Universite de Bourgogne (2008)
10. Chahl, J., Mizutani, A.: Biomimetic attitude and orientation sensors. IEEE Sensors Journal 12, 289–297 (2012)
11. Berry, H.G., Gabrielse, G., Livingston, A.E.: Measurement of the stokes parameters of light. Applied Optics 16, 3200–3205 (1977)
12. Scaramuzza, D., Siegwart, R.: A practical toolbox for calibrating omnidirectional cameras. In: Vision Systems Applications (2007)
13. Coemans, M., vos Hzn, J., Nuboer, J.: The relation between celestial colour gradients and the position of the sun, with regard to the sun compass. Vision Research 34, 1461–1470 (1994)
14. Berry, M.V., Dennis, M.R., Lee Jr., R.L.: Polarization singularities in the clear sky. New Journal of Physics 6, 162 (2004)